



**HAL**  
open science

# A physical approach towards controlling the microstructure of metakaolin-based geopolymer foams

Asmaa Kaddama, Olivier Pitois

## ► To cite this version:

Asmaa Kaddama, Olivier Pitois. A physical approach towards controlling the microstructure of metakaolin-based geopolymer foams. *Cement and Concrete Research*, 2019, 124, pp.105807. 10.1016/j.cemconres.2019.105807 . hal-02883738

**HAL Id: hal-02883738**

**<https://enpc.hal.science/hal-02883738>**

Submitted on 29 Jun 2020

**HAL** is a multi-disciplinary open access archive for the deposit and dissemination of scientific research documents, whether they are published or not. The documents may come from teaching and research institutions in France or abroad, or from public or private research centers.

L'archive ouverte pluridisciplinaire **HAL**, est destinée au dépôt et à la diffusion de documents scientifiques de niveau recherche, publiés ou non, émanant des établissements d'enseignement et de recherche français ou étrangers, des laboratoires publics ou privés.

# A physical approach towards controlling the microstructure of metakaolin-based geopolymer foams

Asmaa Kaddami and Olivier Pitois\*

*Université Paris Est, Laboratoire Navier, UMR 8205 CNRS – École des Ponts ParisTech – IFSTTAR  
cité Descartes, 2 allée Kepler, 77420 Champs-sur-Marne, France.*

\*corresponding author:

Olivier Pitois,

Université Paris Est, Laboratoire Navier, UMR 8205 CNRS – École des Ponts ParisTech – IFSTTAR  
cité Descartes, 2 allée Kepler, 77420 Champs-sur-Marne, France.

[olivier.pitois@ifsttar.fr](mailto:olivier.pitois@ifsttar.fr)

Keywords: Geopolymer, foam, lightweight, aerated, microstructure

Abstract:

Geopolymer foams are promising sustainable lightweight materials combining insulation efficiency with interesting mechanical and fire resistance properties. Controlling their pore size remains challenging because intrinsic foam aging processes act before hardening. We highlight a physical approach to counteracting aging processes in fresh geopolymer foams and to maintaining the pore morphology that has been set initially by mixing metakaolin suspension with precursor aqueous foam. More precisely, it is shown that arrest of foam aging can be achieved if solid particle concentration in the suspension is larger than a critical value which is proved to depend on both bubble size and gas volume fraction. This behavior is understood through the jamming transition occurring for the metakaolin suspension when confined in the foam network, providing significant solid elasticity against bubble motions. The general significance of the reported result makes it useful, as a complement to chemical formulation, for designing morphology-controlled geopolymer foams.

## 1. Introduction

Geopolymers [1] are potentially interesting construction materials, offering significant advantages in terms of CO<sub>2</sub> reduction, as compared to traditional Portland cement, and combining

mechanical strength with fire resistance. Geopolymer foams are promising sustainable lightweight materials providing thermal insulation properties [2]. For such materials, the higher the air fraction, the higher the thermal insulation capacity. Other properties, such as acoustical properties for example, are highly dependent on the microstructure of the materials, i.e. the way the solid matrix is distributed at the local scale. To this respect, the size of pores and apertures connecting the pores are crucial morphological parameters to control acoustics [3,4].

Controlling the pore distribution in light geopolymer foams is however a difficult task, whatever the foaming method that is used to prepare the fresh material: chemical foaming (gas is released through chemical reactions), pre-made foam (a so-called precursor aqueous foam is prepared separately before mixing with the geopolymer suspension), or air entrainment. The main reason for such an issue is related to intrinsic aging of liquid foams through the three following processes [5]: (i) drainage is caused by density difference between air bubbles and the suspension, (ii) ripening is a gas transfer from smaller bubbles to bigger bubbles, and (iii) coalescence refers to thin film breakage between two neighbor bubbles. The magnitudes of those processes depend on various parameters, such as bubble size, gas content, surfactant type and concentration. In principle, the use of appropriate surfactant allows for the coalescence process to be counteracted. Ripening and drainage are expected to be partly counteracted by increasing significantly the viscosity of the suspension: interstitial liquid flow is slowed down and associated bubble motions are dampened. Attempt to apply such a strategy has been made recently by Hajimohammadi et al.[6] for example. Equivalently, the time during which aging processes have to be counteracted can be advantageously reduced by accelerating the geopolymerization reaction. This can be achieved for example by storing the suspension at moderate temperature before introducing air [7]. However, those approaches do not guaranty control of the pore morphology, which remains challenging for geopolymer foams, especially for foam with high air content.

In this paper we propose a new approach to counteracting aging processes of fresh geopolymer foams and to maintaining the microstructure that has been set initially by mixing metakaolin suspension with precursor aqueous foam. It is highlighted that arrest of foam aging can be achieved if solid particle concentration in the suspension is larger than a critical value which is proved to depend on both bubble size and gas volume fraction. In the following, we describe the materials and methods used in this study (section 2). In particular we present our foaming method allowing to prepare foams with chosen bubble size, gas volume fraction and suspension composition. Then we present (section 3) and we interpret (section 4) our results, before to conclude (section 5).

## 2. Materials and methods

### 2.a. Materials

We used an activating solution prepared by mixing NaOH solution (mass concentration  $C_w = 0.35$ ) with a solution containing  $\text{Na}_2\text{O}$  ( $C_w = 0.08$ ) and  $\text{SiO}_2$  ( $C_w = 0.27$ ) provided by MERCK KGaA, and water. The density is  $\rho_\ell = 1400 \text{ kg/m}^3$  and the chemical composition is given by molar ratios  $\text{H}_2\text{O}/\text{Na}_2\text{O} = 14.68$  and  $\text{SiO}_2/\text{Na}_2\text{O} = 1.01$ . The shear viscosity of the activating solution has been measured to be  $\mu_0 \cong 0.069 \text{ Pa}\cdot\text{s}$ .

Metakaolin (MK) particles were provided by AGS Minéraux (France): Argical M 1200s. Chemical compositions:  $\text{SiO}_2$  55.0%,  $\text{Al}_2\text{O}_3$  39.0%,  $\text{Fe}_2\text{O}_3$  1.8%,  $\text{TiO}_2$  1.5%,  $\text{K}_2\text{O}+\text{Na}_2\text{O}$  1.0%,  $\text{CaO}+\text{MgO}$  0.6%. As provided by the supplier: BET specific surface area is equal to  $19 \text{ m}^2/\text{g}$  and mass average diameter is approximately  $d_p \approx 2 \text{ }\mu\text{m}$ . A picture of the particles as observed with a microscope is presented in [Figure 1a](#). Among the numerous particles with size 1-5 $\mu\text{m}$ , one can see particles with size close 10  $\mu\text{m}$ , and several large particles with size up to 30  $\mu\text{m}$ . Their shape is rather irregular and many particles have plate-like shape. Their density is  $\rho_{MK} = 2200 \text{ kg/m}^3$ .

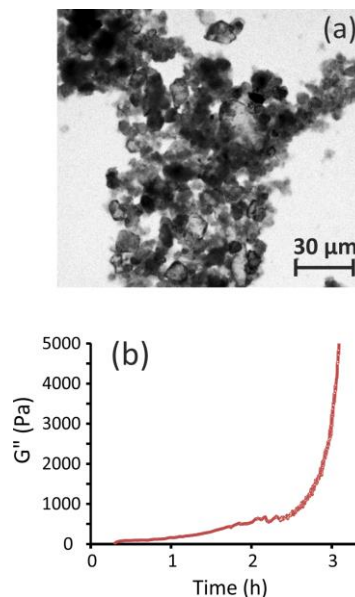


**Figure 1:** (a) Metakaolin particles as observed with a microscope, after drying a dilute water suspension. (b) Loss (viscous) modulus of the paste ( $L/S = 1.5$ ) measured by oscillatory shear rheometry as a function of time. The deformation is equal to  $4 \cdot 10^{-4}$ , which is small enough to not perturbing the geopolymer setting at early age, and the frequency is equal to 1 Hz.

The activated MK suspensions were prepared by mixing a mass  $m_\ell$  of the activating solution with a mass  $m_{MK}$  of metakaolin particles. The suspension is characterized by the ratio  $L/S =$

$m_\ell/m_{MK}$ . Alternatively, the liquid/solid composition can be expressed by the volume fraction of solid particles in the liquid:

$$\varphi_p = \left(1 + \frac{\rho_{MK}L}{\rho_\ell S}\right)^{-1} \quad (\text{eq. 1})$$

For the present study we have prepared more than 200 suspensions, each of them being characterized by  $1.75 \lesssim (L/S)_0 \lesssim 4$  and  $0.14 \lesssim \varphi_{p,0} \lesssim 0.27$ . The subscript "0" refers to the initial value for those parameters, that is, corresponding to the preparation of the suspension. The chemical composition of those samples is given by Si/Al and  $\text{Na}_2\text{O}/\text{Al}_2\text{O}_3$  ratios, respectively within the ranges 1.8-2.5 and 1.2-2.7.

The typical setting time for the MK paste was estimated through oscillatory rheometry tests (see [Figure 1b](#)), similarly to previous studies [8,9]. The starting of the geopolymerization process corresponds to the sharp increase of the viscous modulus and it is observed after more than two hours. Moreover, the viscous modulus of the paste is almost unchanged during the first hour of aging.

The following surfactants were used as received:

- **AlphaFoamer**<sup>®</sup> (ammonium alkyl ether sulfate), *anionic*, M = 277 g/mol, provided by Stepan.
- **Bio-Terge**<sup>®</sup> AS-40K (sodium C14-16 olefin sulfonate), *anionic*, M = 315 g/mol, provided by Stepan.
- **Steol**<sup>®</sup> 270 CIT (Sodium Laureth Sulfate), *anionic*, M = 382 g/mol, provided by Stepan.
- **SDS** (Sodium dodecyl sulfate), *anionic*, M = 288 g/mol, provided by Sigma-Aldrich.
- **CTAB** (cetyltrimethylammonium bromide), *cationic*, M = 364 g/mol, provided by Sigma-Aldrich.
- **TTAB** (tetradecyltrimethylammonium bromide), *cationic*, M = 336 g/mol, provided by Sigma-Aldrich.
- **TEGO**<sup>®</sup> **Betain** F50 (cocamidopropyl betaine), *amphoteric*, M = 343 g/mol, provided by Evonik.
- **Triton**<sup>™</sup> X-100 (octylphenol ethoxylate), *nonionic*, M = 625 g/mol, provided by Sigma-Aldrich.
- **Tween**<sup>®</sup> **20** (polyethylene glycol sorbitan monolaurate), *nonionic*, M = 1225 g/mol, provided by Acros.
- **Tween**<sup>®</sup> **80** (polyethylene glycol sorbitan monooleate), *nonionic*, M = 1310 g/mol, provided by Acros.
- **Glucopon**<sup>®</sup> 225 DK (alkyl polyglycoside), *nonionic*, M = 420 g/mol, provided by BASF.

## 2.b. Stability of foam made from the activating solution

Foamability and foam stability of the activating solution have been evaluated in the presence of the surfactants presented above. Each surfactant solution is obtained by adding a quantity of surfactant in water which is then added (mass proportions 50/50) to the activating solution described previously, resulting in 8 mL of the mixture, introduced into a vessel of volume  $V_{vessel} = 50$  mL. The surfactant quantity is chosen such that the resulting concentration is well above the critical micellar concentration in pure water (the resulting surfactant concentrations are presented in Figure 3). The vessel is closed and the solution is agitated by hand during 20s. The volume of foam produced  $V_{foam}$  is measured right after agitation ( $t=0$ ) and at time  $t = 1$ h.

## 2.c. Production of controlled metakaolin foams

In broad outline, metakaolin foams are produced by mixing precursor aqueous foam with the metakaolin (MK) suspension described previously. The production process consists of two steps (as described in Figure 2): (1) production of the precursor aqueous foam, (2) mixing of the precursor aqueous foam with the MK suspension and in-line filling of the resulting MK fresh foam in a vessel.

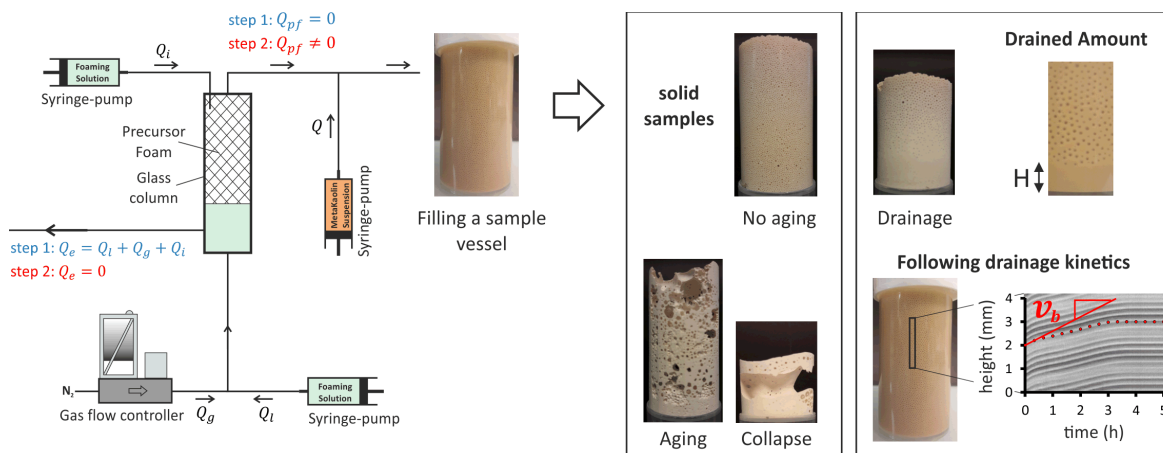


**Figure 2:** (Left) Complete scheme of the foaming device used to produce the fresh MK foams. The device consists in two main consecutive steps: (step 1) Monodisperse aqueous foam production using microfluidics. The control of the bubble size is made at this step. (step 2) The precursor foam is then pushed with the MK suspension through a static mixing device and the sample vessel is filled. The proportions of precursor foam/MK suspension are controlled by tuning their volume flow rates, and these parameters have been shown to set also the final pore volume fraction in the solid samples. (Middle) Examples of solid samples made with the presented method: “No aging” corresponds to samples for which initial morphology has been maintained. (Right) Example of sample for which drainage has occurred, resulting in material with vertical density gradient. The drained amount of MK suspension can be measured from the height  $H$  observed at the bottom of the solid samples. Drainage kinetics can be assessed from the bubbles rising velocity  $v_b$  as measured in a spatio-temporal picture (a vertical pixels line is extracted at the same position from the pictures of the sample at different times and it is used to construct a new picture where height corresponds to real space and horizontal corresponds to time). The light and dark lines therefore correspond to the upward motion of the bubbles. Note that the reported

*drainage velocity corresponds to the maximal value measured over times  $t < 1h$ , so it is not influenced by the setting of the paste.*

Step 1: Aqueous foam is generated by pushing both gas (nitrogen) and foaming liquid (aqueous solution made from the surfactants described in section 2.a) through a T-junction (see [Figure 2](#)). Gas volume flow rate  $Q_g$  is set within the range 0.1-10 mL.min<sup>-1</sup> by using a gas mass flow controller. The foaming solution is pushed at volume flow rate  $Q_l$  thanks to a syringe pump. Tuning the flow rates ratio  $Q_g/Q_l$  through a T-junction with a circular cross-section of diameter 1.6 mm was found appropriate to produce bubbles with diameters  $D_b$  ranging between 800  $\mu\text{m}$  and few millimeters. In order to obtain smaller bubble sizes, typically from 400  $\mu\text{m}$  to 800  $\mu\text{m}$ , the internal diameter of the T-junction was reduced by inserting a glass capillary with external diameter fitting T-junction's walls. Following the same principle, even smaller bubbles (i.e.  $D_b \approx 200 \mu\text{m}$ ) have been produced by reducing the cross-section of the glass capillary. This was achieved by using a micropipette puller (Vertical Micropipette Puller P-30 from Sutter Instrument). Note that reducing the bubble size involves decreasing strongly the flow rates' operating range:  $Q_g \approx 5 \text{ mL.min}^{-1}$  for the large bubbles,  $Q_g \approx 0.5 \text{ mL.min}^{-1}$  for small bubbles. Generated bubbles are continuously collected into a vertical glass column (see [Figure 2](#)). The average bubble diameter  $D_b$  is measured using a camera focused at the wall of the column. As the bubble generation process requires a significant amount of liquid (i.e. typically 50% liquid vs 50% gas), and because the column is initially filled with foaming solution, excess liquid is withdrawn from the column thanks to an overflow outlet (as indicated by flow rate  $Q_e$  in [Figure 2](#)). Note that for foam made with bubble size  $D_b \geq 500 \mu\text{m}$ , ripening turns out to be insignificant over the duration of the production step, so monodisperse precursor aqueous foams were obtained. In contrast, smaller bubble sizes were observed to evolve during the production step because of the ripening process. This can be explained by both the increase of the ripening rate for smaller bubbles [5] and the decrease of the production rate (larger time required to produce the same volume of foam) for smaller bubbles. Such an evolution was efficiently counteracted by using perfluorohexane as a saturating vapor in the bubbling gas [10]. Note that for such cases, the ripening process is permanently counteracted. For all cases, foam stability was improved during the whole foaming process by pouring foaming solution from the top of the column (see [Figure 2](#)) with small flow rate  $Q_i$  (typically  $0.1 \times Q_g$ ). As a result of those imbibition/drainage conditions, constant gas volume fraction  $\phi_0$  ranging from 0.98 to 0.99 was obtained over the most part of the foam column (i.e. except for the 3-4 cm at the bottom [5]). Note that a quantitative control of  $\phi_0$  can be achieved by tuning  $Q_i$  thanks to predictions from numerical simulations such as those reported in Gorlier et al. [11] for example.

Step 2: After production of the required precursor foam volume, the latter is pushed with the MK suspension through a static mixer (flow focusing device and classical helical geometries). The gas volume fraction within the resulting MK foam can be adjusted by tuning the ratio of flow rates for the precursor foam ( $Q_{pf}$ ) and the MK suspension ( $Q_{MK}$ ):

$$\phi_g = \frac{\phi_0 \times Q_{pf}}{Q_{pf} + Q_{MK}} \quad (\text{eq. 2})$$

Similarly, the volume fraction of MK particles contained in the interstitial suspension is given by:

$$\varphi_p = \frac{\varphi_{p,0} \times Q_{MK}}{(1 - \phi_0) \times Q_{pf} + Q_{MK}} \quad (\text{eq. 3})$$

As expressed by eq.3, our foaming process involves the dilution of the MK suspension. Equations 2 and 3 are used to define the targets for  $\phi_g$  and  $\varphi_p$ , but because of possible gas compressibility effect, the actual flow rate of the precursor foam may be different from the targeted value. Therefore, the actual values for  $\phi_g$  and  $\varphi_p$  obtained a posteriori for each produced sample have been calculated as follows: the gas volume fraction is determined from the measured density of the fresh MK foam,  $\rho_{MK,f}$ , and the targeted value for the interstitial suspension,  $\rho_{susp} = [Q_{MK}(\varphi_{p,0} \times \rho_{MK} + (1 - \varphi_{p,0}) \times \rho_\ell) + Q_{pf}(1 - \phi_0) \times \rho_{water}] / [Q_{MK} + Q_{pf}(1 - \phi_0)]$ :  $\phi_g = 1 - \rho_{MK,f} / \rho_{susp}$ . From the actual  $\phi_g$  value the actual precursor foam flow rate is then determined by  $q_{pf} = Q_{MK} \phi_g / (\phi_0 - \phi_g)$ , as well as the resulting MK volume fraction from eq. 3. In practice, however, the measured values were found to be very close to the targeted values. In the following we report the measured values for  $\phi_g$  and  $\varphi_p$ , which were found respectively within the ranges 0.63-0.92 and 0.11-0.25 (equivalently, the L/S values were within the range 1.8-5).

The resulting fresh foam is continuously pushed in a sample vessel of diameter 26 mm and height  $H_0 = 50$  mm (see [Figure 2-left](#)). Typical volume flow rates for the production of the studied samples are of the order of 10 mL/min. The vessel is filled to the top and then closed.

#### 2.d. Following the aging of the fresh MK foam

The aging of the fresh MK foams was studied by taking pictures at the wall of the vessel, right after filling. Such a picture is shown in [Figure 2](#). Occurrence of ripening or drainage was rather easy to follow thanks to adequate light contrast between the bubbles (dark) and the MK suspension

(light). The drainage process was quantified by measuring the bubbles rising velocity  $v_b$ . The latter was determined from spatio-temporal plots, such as the one presented in [Figure 2-right](#). Note that the drainage process generally exhibits a regime of constant velocity, whose duration depends on the various parameters of the system, then the drainage velocity decreases because of the intrinsic foam properties or because the MK paste starts to set. In the following we report the maximal drainage velocity measured at the beginning of the drainage process, so it not influenced by the setting of the paste. Alternatively, the amount of drained suspension can be assessed in the solid sample by the height  $H$  in [Figure 2-right](#). The fraction of drained suspension is therefore given by ratio  $H/[(1 - \phi_g)H_0]$ .

## 2.e. Rheology

Rheometry has been performed (Malvern kinexus ultra+), either with MK suspensions or fresh MK foams. For suspensions, we used two different geometries: vane-in-cup (striated cup of diameter/depth: 37 mm/62.5 mm, 4 blades vane of diameter/length: 25 mm/50 mm) and plane/plane (sandblasted disk, diameter/gap: 60 mm/0.5 mm). Elastic and loss shear moduli were measured in the cup-in-vane geometry, just after the filling step, at a fixed shear strain amplitude  $\varepsilon = 4 \cdot 10^{-4}$  and at a fixed frequency of 1Hz (such conditions allow for the elastic modulus to be measured without perturbing the material [8,9]). The maximum stress for flow start-up was measured in the plane-plane geometry, at a constant shear rate  $\dot{\varepsilon} = 10^{-3} \text{ s}^{-1}$ , after pre-shearing at  $50 \text{ s}^{-1}$ . The viscosity was determined from a plot of shear stress versus shear rate, for shear rates increasing from  $10^{-3}$  to  $50 \text{ s}^{-1}$  within 3 minutes (logarithmic progression).

For fresh foams, we used the cup-in-vane geometry, just after the filling step, at a fixed shear strain amplitude  $\varepsilon = 4 \cdot 10^{-4}$  and at a fixed frequency of 1Hz. Recently, experimental work performed on the rheology of foams made with complex elastic media has shown how to deduce the elastic modulus  $G_0$  of the interstitial material from the rheology of the foam [11–14]. Generic curves  $G(\phi_g, Ca_{el})$  are provided in reference [11], where  $Ca_{el} = G_0 D_b / 2\gamma$  is the elastic capillary number, with  $\gamma \cong 27 \text{ mN/m}$  the surface tension of the liquid/gas interface, which allows for  $G_0$  to be deduced.

## 2.f. X-ray tomography

Images of small samples (i.e. 5x5x10 mm) were obtained with a Ultratom scanner from RX solutions. Measurement involved a Hamamatsu L10801 X-ray source (160 kV) and a Paxscan Varian 2520 V at-panel imager. All scans were performed at 60 kV and 85  $\mu\text{A}$ . Frame rate was 3 images per second and 12 images were averaged to produce one projection (the resulting effective exposure time was therefore 4s). 3D tomographic reconstruction was performed with the X-Act commercial

software developed by RX-Solutions. Voxel size for the obtained images was 5  $\mu\text{m}$ . Pores appeared black on the reconstructed images and interstitial geopolymer solid was light grey. This allowed us to analyze the images with the freeware ImageJ program [15] to compute the pore size distribution: First, a closing filter from MorphoLibJ plugin [16] with a 2 voxel-radius ball element was applied to reduce noise from the images. Then, image threshold was calculated using the Otsu method [17]. 3D Watershed from MorphoLibJ was applied, then 1-voxel dilatation filter. Finally, 3D Object Counter plugin returned the volume ( $V_{p,i}$ ) of each pore, from which the equivalent pore diameter  $(6V_{p,i}/\pi)^{1/3}$  was calculated.

### 3. Results

Foaming of the activating solution has been evaluated with several surfactants, as shown in [Figure 3](#). Several surfactants do not allow foaming of such a solution, see Steol (anionic) or Tween and Triton (nonionic) for example. Note that such surfactants are sometimes used for foaming purpose with geopolymer solutions [6,7,18–22]. Note also that precipitates were sometimes observed (Tween 80 and SDS). Other surfactants allow good foaming but poor stability, see CTAB (cationic) and TTAB (cationic) for example. Finally, several surfactants allow good foaming as well as good stability, i.e. the foam volume is unchanged after 1 hour, see Alphafoamer (anionic) and Glucocon (nonionic) for example.

Results for rheometry performed with the surfactant MK suspensions ( $L/S = 2.40 \pm 0.15$ , or equivalently  $\varphi_p = 0.20 \pm 0.02$ ) are now presented (see [Figure 4](#)). Note that the chosen surfactant concentrations correspond to concentrations resulting from the mixing step described in section 2.c, where surfactant is introduced with the foaming liquid contained in the precursor but it is not present in the initially prepared MK suspension. Distinct behaviors are observed as surfactant is introduced in the suspension. For several surfactants, the maximum shear stress exhibited by the start-flow curve is drastically increased with respect to the surfactant-free suspension. This is the case for Steol and TTAB, where the stress ratio is close to 20 and 15 respectively. This behavior is presumed to be related to a strong interaction of those surfactants with the aluminosilicate surface [23,24]. On the other hand, several surfactants have almost no influence on the MK suspension rheology, i.e. a stress ratio close to unity, see for example SDS, Glucocon or Tween. Finally, Bioterge and TegoBetain have intermediate behavior, characterized by a stress ratio close to 3-4.

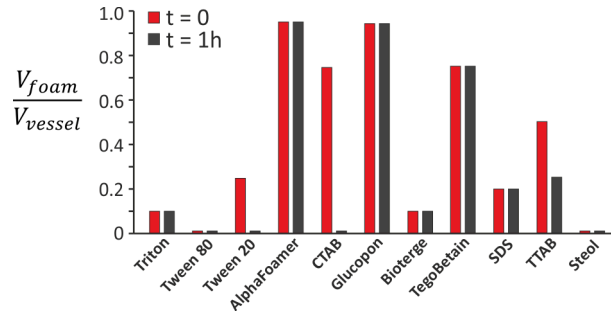


**Figure 3:** Volume of foam ( $V_{foam}$ ) made from the activating solution and surfactant (as indicated in the horizontal axis),  $t=0$  and  $t=1h$  after shaking the sample vessel ( $V_{vessel} = 50$  mL). Surfactant concentration depends on the sample: 6 g/L for Triton, 1.5 g/L for Tween 80, 2 g/L for Tween 20, 20 g/L for Alphafoamer, 15 g/L for CTAB, 10 g/L for Glucocon, 6 g/L for Bioterge, 30 g/L for TegoBetain, 20 g/L for SDS, 15 g/L for TTAB, 8 g/L for Steol (see section 2.a for more details about the surfactants).

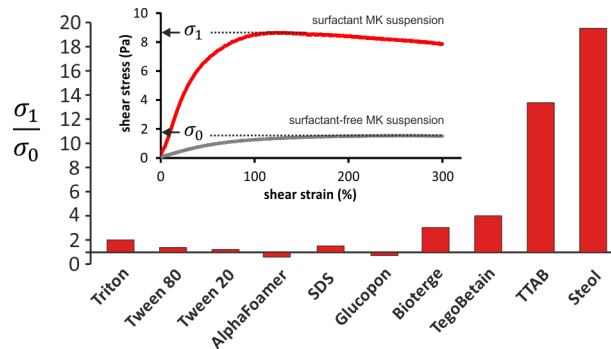
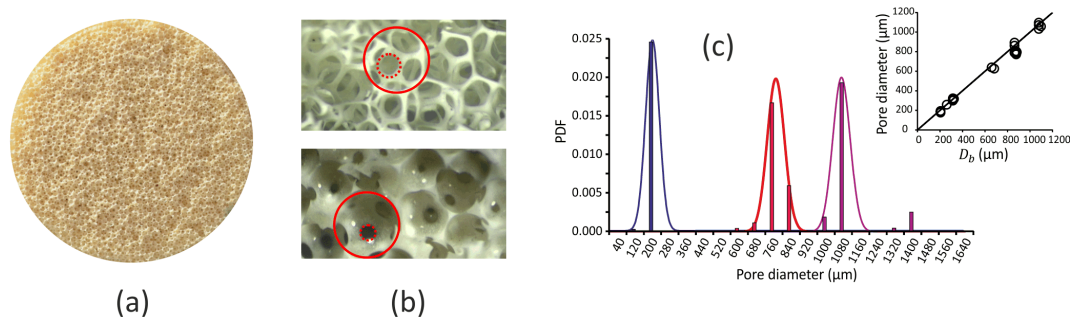


**Figure 4:** Ratio of the maximum shear stresses measured for MK suspensions, characterized by  $L/S = 2.40 \pm 0.15$  ( $\phi_p = 0.20 \pm 0.02$ ), with ( $\sigma_1$ ) and without ( $\sigma_0$ ) surfactant during a start flow experiment at constant shear rate ( $\dot{\epsilon} = 10^{-3} s^{-1}$ ), as shown in the inset for TegoBetain. Surfactant concentration depends on the sample: 0.2 g/L for Triton, 0.05 g/L for Tween 80, 0.12 g/L for Tween 20, 5 g/L for Alphafoamer, 3 g/L for SDS, 2.3 g/L for Glucocon, 0.04 g/L for Bioterge, 2 g/L for TegoBetain, 2.5 g/L for TTAB, 0.4 g/L for Steol (see section 2.a for more details about the surfactants).

The production of MK foams with the studied surfactants has revealed strong differences. For each case, the targeted values for bubble size and gas volume fraction were 600  $\mu m$  and 0.85 respectively. Several surfactants were found to be inappropriate to produce controlled MK foams with our foaming method. The reasons for such a result differ depending on the surfactant. Strong collapse of MK foam (see Figure 2-Middle) was observed for Triton, SDS and TTAB, right after the aqueous foam was mixed with the MK suspension. Increasing the surfactant concentration did not fix the stability issue. This is not surprising as those surfactants were also found to provide poor foam stability with the activating solution (see Figure 3). For Steol, additional issue arised from the drastically increased shear stress presented in the previous paragraph (see Figure 4): aqueous foam and MK Steol suspension did not mix very well and the resulting MK foams were found to be very

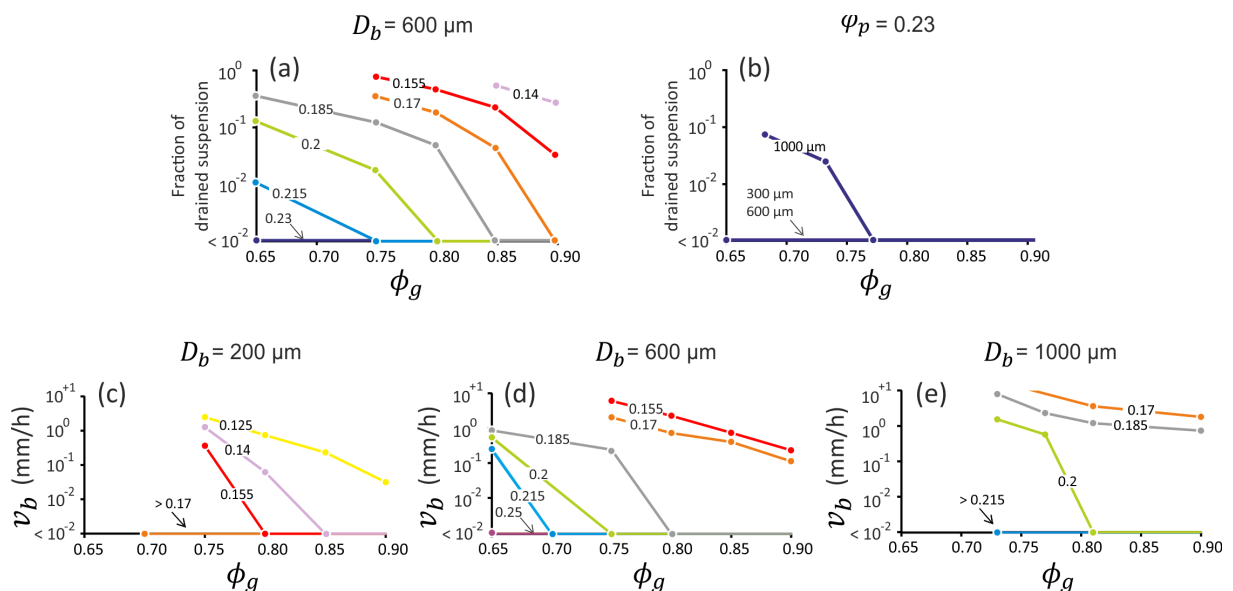
inhomogeneous and exhibited strong aging. Tween aqueous foams (precursor foams) showed coalescence issues when transported through the tubes of the production setup, upstream of the mixing stage. This issue was fixed by increasing the liquid content in the precursor foam, but this additional quantity of liquid appeared to be detrimental to the fresh MK foam, where strong aging effects were observed. MK foams obtained from Bioterge, TegoBetain and Aphafoamer exhibited significant aging before setting, and the resulting solid foams were found to have uncontrolled pore size (see Figure 2-Middle). Moreover, the corresponding hardened geopolymer foams were found to be fragile. MK foams produced with Glucopon showed remarkable stability properties against coarsening. Note also that for the L/S value studied, drainage and ripening processes were efficiently counteracted. Actually, for all the samples made with Glucopon, ripening was not observed as soon as drainage was efficiently counteracted. In other words, drainage is the most critical aging process within our experimental conditions, and we present a full study of drainage in the following. We recall that perfluorohexane was used to prevent ripening during the preparation of the precursor aqueous foam with bubble size smaller than 500  $\mu\text{m}$ , so we are not able to discuss about ripening of fresh MK foams for that range of bubble sizes.

Figure 5 shows that the resulting pore size distributions are very narrow due to the use of monodisperse precursor foam and to the absence of coarsening. The interesting point is that, within our experimental errors, the resulting pore size is equal to the bubble size in the precursor aqueous foam (see the inset in Figure 5). Such pore size distributions appear to be narrower than previously reported size distributions for open-cell geopolymer foams (see for example references [7,18,20,22,25–30]).



**Figure 5:** Morphology of the solid MK foams. (a) Picture of a sample seen from above ( $D_p \approx 600 \mu\text{m}$ , density =  $250 \text{ kg/m}^3$ ). (b) Close-up of the samples (top:  $800 \mu\text{m}$ ,  $50 \text{ kg/m}^3$ ; bottom:  $800 \mu\text{m}$ ,  $350 \text{ kg/m}^3$ ). Circles show pores (solid line) and apertures between pores (dotted line). (c) Volume-weighted pore size distribution (probability density function) for three samples. The three Gaussian curves are plotted with mean and standard deviation equal to:  $200 \mu\text{m}$  and  $32 \mu\text{m}$ ,  $770 \mu\text{m}$  and  $40 \mu\text{m}$ ,  $1070 \mu\text{m}$  and  $40 \mu\text{m}$ . Inset: Pore size measured in 27 solid samples as a function of bubble size measured in the precursor aqueous foam.

Results for the study of drainage effects for fresh Glucocon MK foams are reported in Figure 6. For a given bubble size  $D_b = 600 \mu\text{m}$ , the fraction of drained suspension (see Figure 2-right) is all the more significant as both the particle volume fraction  $\varphi_p$  (MK particles in the interstitial volume of the foam) and the gas volume fraction are low (see Figure 6a). On the other hand, for  $\varphi_p$  value as high as 0.23, drainage effects could not be revealed over the full range of investigated  $\phi_g$  values. However, drainage effects can be observed for  $\varphi_p = 0.23$  if the bubble size is increased up to 1 mm (see Figure 6b), showing that drainage of fresh MK foams is controlled at the same time by parameters  $\varphi_p$ ,  $\phi_g$  and  $D_b$ . This behavior is also evidenced by Figures 6c-e, where the drainage velocity is reported as a function of  $\phi_g$ , for several  $\varphi_p$  and  $D_b$  values. It is shown here that bubble size is a crucial parameter to control drainage kinetics: foam made with the same MK suspension ( $\varphi_p = 0.17$ ) is draining at a velocity close to 1 mm/h when  $D_b = 600 \mu\text{m}$ , but drainage is insignificant (i.e. the drainage velocity is smaller than  $10^{-2}$  mm/h) if the bubble size is reduced to  $D_b = 200 \mu\text{m}$ . Figure 7 shows the drainage behavior for all the samples, i.e. insignificant or significant drainage velocity, by plotting  $\varphi_p$  as a function of  $\phi_g$  for all the studied bubble sizes  $D_b$ . One can see that: (i) For a given set of values  $\phi_g$  and  $D_b$ , increasing  $\varphi_p$  allows for drainage to be stopped; (ii) For a given set of values  $\varphi_p$  and  $D_b$ , increasing  $\phi_g$  allows for drainage to be stopped; (iii) For a given set of values  $\varphi_p$  and  $\phi_g$ , decreasing  $D_b$  allows for drainage to be stopped. An attempt to describe quantitatively the drainage behavior is presented in the following discussion.



**Figure 6:** Drainage of MK foams. (a,b) Fraction of drained MK suspension, as measured at the bottom of the sample after hardening, as a function of gas volume fraction  $\phi_g$ : (a) for a given bubble size  $D_b$  and several particle volume fractions  $\phi_p$  (as indicated by the values reported for each curve), (b) for a given particle volume fraction  $\phi_p$  and several bubble sizes  $D_b$  (as indicated by the values reported for each curve). (c-e) Drainage velocity  $v_b$  measured for fresh MK foams made with bubbles of different sizes: (c)  $D_b = 200 \mu\text{m}$ , (d)  $D_b = 600 \mu\text{m}$ , (e)  $D_b = 1000 \mu\text{m}$ . Each curve is characterized by a given particle volume fraction  $\phi_p$ , as indicated by the values.

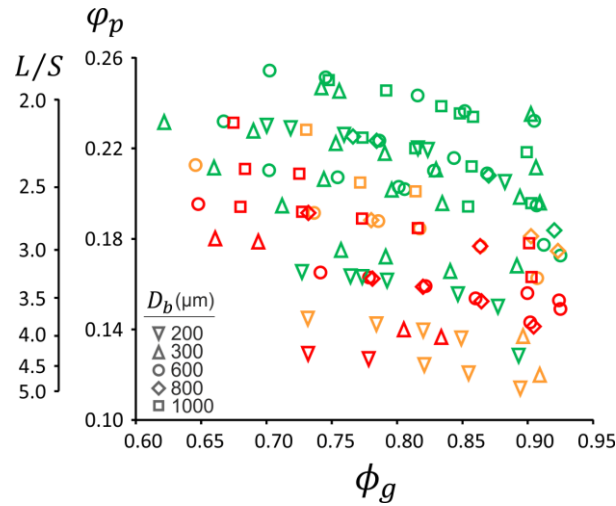


**Figure 7:** Drainage behavior of fresh MK foams as a function of the studied parameters  $\phi_p$  (or equivalently  $L/S$ ),  $\phi_g$  and  $D_b$ . Green symbols represent samples for which drainage is insignificant (i.e. the drainage velocity is lower than  $10^{-2} \text{ mm/h}$ ). Orange symbols correspond to drainage limited to the periphery of the sample, whereas red symbols correspond to significant drainage.

#### 4. Discussion

Results show that only a small number of surfactants are suitable for producing metakaolin-based foams, and in fact only Glucopon was found efficient to stabilize the foam films over the full period preceding the hardening step, and potentially to control the final pore size. However, it appears evident that, although required, the use of the latter surfactant is not sufficient for controlling the morphology of the hardened geopolymer foam. This is mainly because of the drainage process induced by the density difference between gas bubbles and the metakaolin suspension. The ripening process, which results from gas exchange between bubbles, was not observed for samples which were found to be stable with respect to drainage (see Figure 5), so we focus on the drainage process in the following.

The drainage of foams made from particle suspension has been studied recently [31–33]. A major result for such complex liquid foams is that the drainage velocity can be understood from the

particle volume fraction  $\phi_p$  and a parameter  $\lambda$  called the confinement parameter. This parameter compares the particle size  $d_p$  to the size of constrictions in the foam network, and expresses for monodisperse liquid foams [34] as:

$$\lambda = C(\phi_g) \frac{d_p}{D_b} \quad (\text{eq. 4})$$

with  $C(\phi_g) = [1 + 0.57(1 - \phi_g)^{0.27}] / [0.27(1 - \phi_g)^{1/2} + 3.17(1 - \phi_g)^{2.75}]$ . Note that for a given particle size, the confinement parameter increases when the gas volume fraction increases or when the bubble size decreases. Using equation 4,  $\lambda$  values are calculated for all the data presented in [Figure 7](#), and a new plot is presented as a function of  $\lambda$  in [Figure 8](#). Note that we used  $d_p = 2 \mu\text{m}$  in equation 4 although the range of particle sizes has been shown to be spread (see section 2.a and [Figure 1a](#)). It appears that the drainage behavior can be understood through a single parameter, namely the critical particle volume fraction  $\phi_p^*(\lambda)$ , above which the drainage process is insignificant. It is to recall that drainage velocities have been measured at the very early age of aging, so the reported drainage behavior is not at all influenced by the intrinsic setting properties of the pastes. On the contrary, this behavior can be interpreted as the collective jamming of the solid particles in the narrow and tortuous foam channels: with respect to jamming of the bulk suspension at solid volume fraction  $\phi_p^*(0)$ , jamming concentration decreases significantly when confinement effects are significant in the foam interstitial space, i.e.  $\phi_p^*(\lambda)$  is a decreasing function of  $\lambda$ . [Figure 8](#) shows that  $\phi_p^* = 0.12\lambda^{-1/4}$  within the investigated range of  $\lambda$  values. Two remarks should be made at this point. First, the measured  $\phi_p^*$  values are significantly smaller than previously reported values [31,33] for the drainage of foams made with suspensions of spherical particles, i.e. 0.46-0.57. Such a difference can be attributed mainly to the difference in the bulk jamming concentrations of spherical and anisotropic particles, as discussed in more detail in the following. Second, the observed power law behavior for  $\phi_p^*$  as a function of  $\lambda$  does not extend to larger  $\lambda$  values. Indeed, it has been shown that the so-called *particle exclusion transition* occurs for such large  $\lambda$  values [31], where the particles are trapped by the foam channels whereas the suspending liquid is draining.

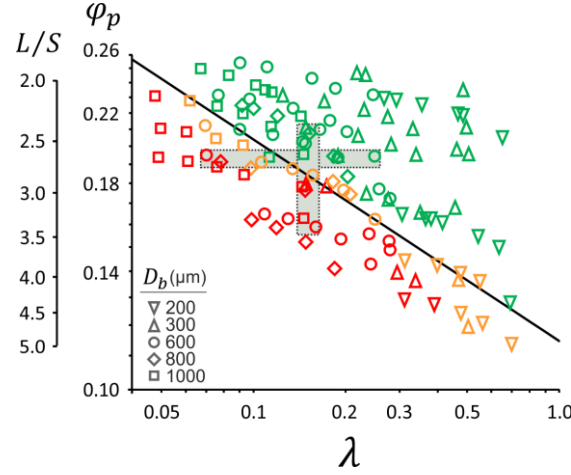


**Figure 8:** Drainage behavior of fresh MK foams as a function of the confinement parameter  $\lambda$  given by equation 4. Note the log-log scales. Green symbols represent samples for which drainage is insignificant (i.e. the drainage velocity is lower than  $10^2$  mm/h). Orange symbols correspond to drainage limited to the periphery of the sample, whereas red symbols correspond to significant drainage. The continuous line corresponds to  $\varphi_p^* = 0.12\lambda^{-1/4}$ . The grey areas (horizontal and vertical) represent series of rheology experiments performed on fresh MK foams in order to estimate the elastic modulus of the foam embedded MK suspension.

Confinement effects are expected to be observed for  $\varphi_p(\lambda) < \varphi_p^*(\lambda)$  through the increase of the effective viscosity  $\mu$  of the MK suspension that is flowing in the foam interstitial network. As shown in the following, the effective viscosity can be deduced from the measured drainage velocity  $v_b$  (see Figure 6c-e). Such a drainage process is conveniently described by the Darcy law:  $v_D = k\rho_{susp}g/\mu$ , where  $k \equiv k(D_b, \phi_g)$  is the foam permeability and  $v_D = \phi_g v_b$  is the Darcy velocity, i.e. the superficial flow velocity [5]. Foam permeability can be found in literature for the studied range of bubble sizes and gas volume fractions [35]:  $k = f(\phi_g) \times D_b^2$ , with  $f(\phi_g) = 0.006 \times (1 - \phi_g)^{3/2} / [1 - 2.7(1 - \phi_g) + 2.2(1 - \phi_g)^2]^2$ , so the effective viscosity of the suspension is related to the drainage velocity by equation 5:

$$\mu = \frac{f(\phi_g) \times D_b^2 \rho_{susp} g}{\phi_g v_b} \quad (\text{eq. 5})$$

The calculated values have been sorted by several  $\lambda$  values (i.e. 0.1, 0.2, 0.35 and 0.6) and plotted as a function of  $\varphi_p$  in Figure 9. Note that (i) for the sake of generality, we refer to the relative viscosity of the suspension  $\mu/\mu_0$  (here  $\mu_0$  is the shear viscosity of the activating solution given in section 2a), and (ii) data of Figure 8, i.e.  $\varphi_p^*(\lambda)$ , now correspond to the divergence of the viscosity. Each  $\lambda$  value is characterized by a well-defined viscosity curve as a function of the particle volume fraction, from  $\mu/\mu_0 \approx 1$  for  $\varphi_p \lesssim 0.1$  to  $\mu/\mu_0 \rightarrow \infty$  for  $\varphi_p \approx \varphi_p^*$ . This means that particle motions are progressively hindered in the foam network as  $\varphi_p$  increases until they are completely blocked at  $\varphi_p^*$ . Moreover,

increasing  $\lambda$  (i.e. decreasing the bubble size or/and increasing the gas volume fraction) is qualitatively equivalent to increasing the particle concentration. These results are now compared to literature. Here we refer to the Krieger-Dougherty relationship [36] for suspensions:

$$\frac{\mu}{\mu_0} = \left(1 - \frac{\varphi_p}{\varphi_p^{max}}\right)^{-B\varphi_p^{max}} \quad (\text{eq. 6})$$

where  $B$  and  $\varphi_p^{max}$  are fitting parameters and correspond respectively to the *Einstein coefficient* (also called *intrinsic viscosity*) and to the particle volume fraction at jamming. The Einstein coefficient takes the value  $B = 2.5$  for spheres, and it is known to increase significantly for anisotropic particles [37].  $\varphi_p^{max}$  is close to 0.6 for monodisperse spheres but it is expected to decrease for anisotropic particles [37]. To this regard, the jamming concentration of MK particles in the activating solution has been measured to be close to 0.3 (see Figure 9). Equation 6 is plotted in Figure 9 by assuming that  $\varphi_p^{max} \cong \varphi_p^*$  and adjusting the coefficient  $B$ . Best agreement was obtained by using  $B = 8-9$  for all of the curves, including the one corresponding to the bulk suspension (the latter has been measured using conventional rheometry), which gives a clear physical picture for drainage in MK fresh foams.

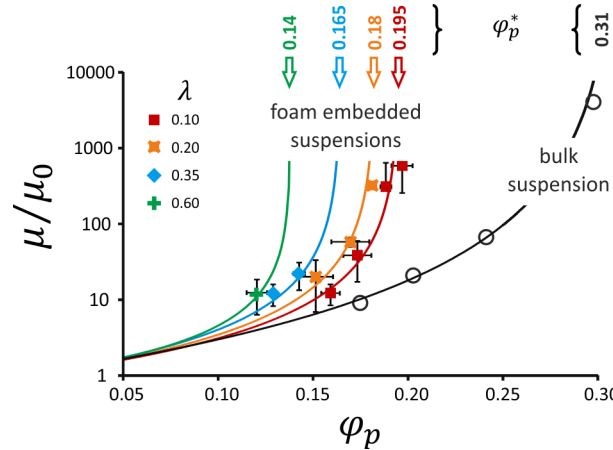


**Figure 9:** Viscosity of the MK suspension (as deduced from the foam drainage velocity) divided by the shear viscosity of the activating solution, as a function of the particle volume fraction. Viscosity values have been sorted by four  $\lambda$  values (0.1, 0.2, 0.35 and 0.6). The shear viscosity of the bulk suspension (as measured by conventional rheometry) is presented for comparison. Values reported for the observed divergence of viscosity (i.e. insignificant drainage) correspond to  $\varphi_p^*(\lambda)$  values presented in Figure 8. Solid lines correspond to equation 6 with parameters  $\varphi_p^{max} \cong \varphi_p^*$  (as indicated for each curve) and  $B = 8$  (for  $\lambda = 0.1$ ), 8.5 (for  $\lambda = 0.2$ ), 9 (for  $\lambda = 0.35$ ), 8.5 (for  $\lambda = 0.6$ ) and 9 (for the bulk suspension).

In the following, we focus on the transition observed for MK foam stability (i.e. [Figure 8](#)) in link with the mechanical strengthening of the foam embedded MK suspension. More precisely, the elastic modulus  $G_0$  of the interstitial material is now deduced from the elastic modulus of the MK foam, as proposed recently [11–14]. Therefore, the elastic modulus  $G(\phi_g, \varphi_p)$  of fresh MK foams has been measured at early age (see section 2e for experimental details) for foams with  $D_b = 600 \mu\text{m}$ , when (a)  $\varphi_p$  is increased while  $\lambda$  is fixed (vertical series shown by the grey area in [Figure 8](#)), and (b)  $\varphi_p$  is fixed while  $\lambda$  is increased (horizontal series shown by the grey area in [Figure 8](#)). Obtained  $G_0$  values are presented in [Figure 10](#). As expected,  $G_0$  increases significantly as a function of  $\varphi_p$  when  $\lambda$  is fixed ([Figure 10a](#)). Note however that the measured increase cannot be explained only by  $\varphi_p$  variation, as shown by comparison with the reported evolution for the bulk MK suspension. The observed strengthening, i.e. a factor 5 with respect to the bulk suspension over the same  $\varphi_p$  range, is induced by confinement provided by the foam network. This is clearly highlighted by [Figure 10b](#), where  $\varphi_p$  is now constant while  $\lambda$  increases: again a strong strengthening is measured when confinement increases in the foam network. For both cases, i.e. either  $\varphi_p$  or  $\lambda$  effect, the transition from unstable to stable MK foam is observed when  $G_0$  exceeds a value close to 150 Pa. Note that interstitial yield stress  $\tau_{y0}$  can be associated to  $G_0$  through the relationship  $\tau_{y0} \cong G_0 \times \varepsilon_c$ , where  $\varepsilon_c$  is the critical deformation for which the interstitial material yields. Therefore, the yield stress of the foam-embedded fresh MK suspension is expected to increase significantly as  $G_0$  increases, that is, as  $\lambda$  increases. This effect is expected to explain the remarkable stability observed for systems characterized by  $\varphi_p \gtrsim \varphi_p^*$ .

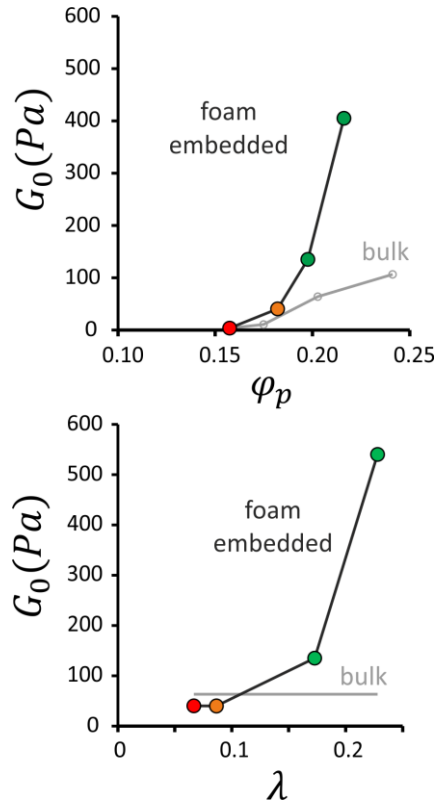


**Figure 10:** Elastic modulus of the foam embedded MK suspension as deduced from rheometry performed on fresh MK foams, (a) as a function of  $\varphi_p$  when  $\lambda = 0.15$  (vertical series shown by the grey area in Figure 8), and (b) as a function of  $\lambda$  when  $\varphi_p = 0.195$  (horizontal series shown by the grey area in Figure 8). Color codes corresponding to Figures 7 and 8 are used, i.e. green symbols correspond to samples that are stable with respect to drainage. Elastic moduli of the bulk MK suspension (measured by conventional rheometry) are presented for comparison.

## 5. Conclusion

Stability of foams produced by mixing metakaolin suspension with precursor aqueous foam has been studied in direct link with surfactant used for foaming, metakaolin concentration, and foam parameters, namely bubble size and gas volume fraction.

First of all, it has been shown that numerous surfactants are not suitable for controlling the foam morphology within those foaming conditions due to (i) strong foam collapse after mixing (Triton, SDS and TTAB), (ii) poor mixing, resulting from surfactant-induced increase of suspension consistency (Bioterge, TegoBetain and Aphafoamer), (iii) insufficient stability of the foam films. However, there are surfactants (Glucopon for example) that allow for all of those issues to be overcome, providing optimal foam films stability over several hours.

It was then shown that the use of the latter surfactant is not sufficient for controlling the morphology of the hardened geopolymer foam. This is mainly due to the drainage process, which is induced by the density difference between the gas bubbles and the metakaolin suspension, and to the ripening process, which results from gas exchange between bubbles.

The drainage velocity has been measured for numerous fresh metakaolin foams, covering a wide range of values for the metakaolin concentration, the bubble size and the gas volume fraction. The major result is that arrest of foam drainage can be achieved if the metakaolin concentration in the suspension is larger than a critical value which depends on both bubble size and gas volume fraction. This behavior is understood through the jamming transition occurring for the metakaolin suspension when confined in the foam network, providing significant solid elasticity against bubble motions. This result is similar to the jamming transition reported for the study of liquid foams made with granular suspensions of spherical particles [31,33], where it was shown that the critical particle concentration first decreases as a function of the so-called confinement parameter (the ratio of particle size to the size of constrictions in the foam network), then increases, and lastly particle jamming is no more reachable. For the latter situation, the particles are still trapped in the foam network but the suspending solution is allowed to drain alone. As a result, for a given particle size and gas volume fraction (typically 90%), there is a bubble size below which drainage cannot be stopped any more through the reported mechanism involving the jamming of the suspension in the foam network. For the metakaolin particles used in this study, this size is expected to be smaller than 200  $\mu\text{m}$  (the smallest bubble size we have studied).

As a consequence of the jamming transition, the ripening process is also arrested. This has been highlighted for bubbles larger than 500  $\mu\text{m}$ . For smaller bubbles, perfluorohexane was used to stop ripening and to control bubble size in the precursor aqueous foam, which did not allow for the ripening process to be studied for those bubble sizes. We stress that additional trials where perfluorohexane was removed from the precursor foam (resulting in less controlled precursor aqueous foam, i.e. more polydisperse) did not induce strong ripening in the fresh MK foam. On the other hand, it is known that ripening is stronger as bubble size decreases, which means that, as for the drainage process, there is a bubble size below which ripening cannot be stopped anymore. Further work focused on ripening could help to clarify that point.

The general significance of the reported result makes it useful, as a complement to chemical formulation, for designing morphology-controlled geopolymer foams. In particular, whatever the

foaming method used to produce those materials, attention should be paid to target bubble sizes and gas volume fractions within the range of values corresponding to the highlighted jammed state.

## Acknowledgment

This work has benefited from French government Grant managed by the Agence Nationale de la Recherche [Grant number ANR-13-RMNP-0003-01].

## References

- [1] J. Davidovits, Geopolymers, *Journal of Thermal Analysis*. 37 (1991) 1633–1656. doi:10.1007/BF01912193.
- [2] Z. Zhang, J.L. Provis, A. Reid, H. Wang, Geopolymer foam concrete: An emerging material for sustainable construction, *Construction and Building Materials*. 56 (2014) 113–127. doi:10.1016/j.conbuildmat.2014.01.081.
- [3] V.H. Trinh, V. Langlois, J. Guilleminot, C. Perrot, Y. Khidas, O. Pitois, Tuning membrane content of sound absorbing cellular foams: Fabrication, experimental evidence and multiscale numerical simulations, *Materials and Design*. 162 (2019) 345–361. doi:10.1016/j.matdes.2018.11.023.
- [4] T.C. Hung, J.S. Huang, Y.W. Wang, K.Y. Lin, Inorganic polymeric foam as a sound absorbing and insulating material, *Construction and Building Materials*. 50 (2014) 328–334. doi:10.1016/j.conbuildmat.2013.09.042.
- [5] I. Cantat, S. Cohen-Addad, F. Elias, F. Graner, R. Höhler, O. Pitois, F. Rouyer, *Foams: Structure and Dynamics*, Oxford University Press, Oxford, 2013.
- [6] A. Hajimohammadi, T. Ngo, P. Mendis, Enhancing the strength of pre-made foams for foam concrete applications, *Cement and Concrete Research*. 87 (2018) 164–171. doi:10.1016/j.cemconcomp.2017.12.014.
- [7] S.M. Cilla, P. Colombo, R.M. Morelli, Geopolymer Foams by Gelcasting, *Ceramics International*. 40 (2014) 5723–5730. doi:10.1016/j.ceramint.2013.11.011.
- [8] A. Poulesquen, F. Frizon, D. Lambertin, Rheological behavior of alkali-activated metakaolin during geopolymerization, *Journal of Non-Crystalline Solids*. 357 (2011) 3565–3571. doi:10.1016/j.jnoncrysol.2011.07.013.
- [9] A. Favier, G. Habert, J.B. D’espinoze De Lacaillerie, N. Roussel, Mechanical properties and compositional heterogeneities of fresh geopolymer pastes, *Cement and Concrete Research*. 48 (2013) 9–16. doi:10.1016/j.cemconres.2013.02.001.
- [10] F.G. Gandolfo, H.L. Rosano, Interbubble Gas Diffusion and the Stability of Foams, *Journal of Colloid and Interface Science*. 194 (1997) 31–36. doi:10.1006/jcis.1997.5067.
- [11] F. Gorlier, Y. Khidas, O. Pitois, Coupled elasticity in soft solid foams, *Journal of Colloid and Interface Science*. 501 (2017) 103–111. doi:10.1016/j.jcis.2017.04.033.
- [12] F. Gorlier, Y. Khidas, A. Fall, O. Pitois, Optimal strengthening of particle-loaded liquid foams, *Physical Review E - Statistical, Nonlinear, and Soft Matter Physics*. 95 (2017) 042604. doi:10.1103/PhysRevE.95.042604.
- [13] F. Gorlier, Y. Khidas, O. Pitois, Elasticity of particle-loaded liquid foams, *Soft Matter*. 13 (2017) 4533–4540. doi:10.1039/c7sm00679a.

- [14] F. Gorlier, Y. Khidas, O. Pitois, Yielding of complex liquid foams, *Journal of Rheology*. 61 (2017) 919–930. doi:10.1122/1.4994786.
- [15] C.T. Rueden, J. Schindelin, M.C. Hiner, B.E. DeZonia, A.E. Walter, E.T. Arena, K.W. Eliceiri, ImageJ2: ImageJ for the next generation of scientific image data, *BMC Bioinformatics*. 18 (2017) 529. doi:10.1186/s12859-017-1934-z.
- [16] D. Legland, I. Arganda-Carreras, P. Andrey, MorphoLibJ: integrated library and plugins for mathematical morphology with ImageJ, *Bioinformatics*. 32 (2016) 3532–3534. doi:10.1093/bioinformatics/btw413.
- [17] N. Otsu, A Threshold Selection Method from Gray-Level Histograms, *IEEE Transactions on Systems, Man, and Cybernetics*. 9 (1979) 62–66. doi:10.1109/TSMC.1979.4310076.
- [18] C. Bai, A. Conte, P. Colombo, Open-cell phosphate-based geopolymer foams by frothing, *Materials Letters*. 188 (2017) 379–382. doi:10.1016/j.matlet.2016.11.103.
- [19] C. Bai, G. Franchin, H. Elsayed, A. Zaggia, L. Conte, H. Li, P. Colombo, High-porosity geopolymer foams with tailored porosity for thermal insulation and wastewater treatment, *Journal of Materials Research*. 32 (2017) 3251–3259. doi:10.1557/jmr.2017.127.
- [20] T.-C. Hung, J.-S. Huang, Y.-W. Wang, Y.-C. Fan, Microstructure and properties of metakaolin-based inorganic polymer foams, *J Mater Sci*. 48 (2013) 7446–7455. doi:10.1007/s10853-013-7559-3.
- [21] A. Hajimohammadi, T. Ngo, P. Mendis, A. Kashani, J.S.J. Van Deventer, Alkali activated slag foams : The effect of the alkali reaction on foam characteristics, *Journal of Cleaner Production*. 147 (2017) 330–339. doi:10.1016/j.jclepro.2017.01.134.
- [22] L. Korat, V. Ducman, The influence of the stabilizing agent SDS on porosity development in alkali-activated fly-ash based foams, *Cement and Concrete Composites*. 80 (2017) 168–174. doi:10.1016/j.cemconcomp.2017.03.010.
- [23] S. Petlitzkaia, A. Poulesquen, Design of lightweight metakaolin based geopolymer foamed with hydrogen peroxide, *Ceramics International*. 45 (2019) 1322–1330. doi:10.1016/j.ceramint.2018.10.021.
- [24] V. Cantarel, D. Lambertin, A. Poulesquen, F. Leroux, G. Renaudin, F. Frizon, Geopolymer assembly by emulsion templating: Emulsion stability and hardening mechanisms, *Ceramics International*. 44 (2018) 10558–10568. doi:10.1016/J.CERAMINT.2018.03.079.
- [25] Z. Zhang, H. Wang, The Pore Characteristics of Geopolymer Foam Concrete and Their Impact on the Compressive Strength and Modulus, *Frontiers in Materials*. 3 (2016) 1–10. doi:10.3389/fmats.2016.00038.
- [26] A. Hajimohammadi, T. Ngo, P. Mendis, J. Sanjayan, Regulating the chemical foaming reaction to control the porosity of geopolymer foams, *Materials and Design*. 120 (2017) 255–265. doi:10.1016/j.matdes.2017.02.026.
- [27] C. Bai, G. Franchin, H. Elsayed, A. Conte, P. Colombo, High strength metakaolin-based geopolymer foams with variable macroporous structure, *Journal of the European Ceramic Society*. 36 (2016) 4243–4249. doi:10.1016/j.jeurceramsoc.2016.06.045.
- [28] E. Papa, V. Medri, D. Kpogbemabou, V. Morinière, J. Laumonier, A. Vaccari, S. Rossignol, Porosity and insulating properties of silica-fume based foams, *Energy and Buildings*. 131 (2016) 223–232. doi:10.1016/j.enbuild.2016.09.031.
- [29] L. Verdolotti, B. Liguori, I. Capasso, A. Errico, D. Caputo, M. Lavorgna, S. Iannace, Synergistic effect of vegetable protein and silicon addition on geopolymeric foams properties, *Journal of Materials Science*. 50 (2014) 2459–2466. doi:10.1007/s10853-014-8801-3.

- [30] G. Samson, M. Cyr, X.X. Gao, Thermomechanical performance of blended metakaolin-GGBS alkali-activated foam concrete, *Construction and Building Materials*. 157 (2017) 982–993. doi:10.1016/j.conbuildmat.2017.09.146.
- [31] B. Haffner, Y. Khidas, O. Pitois, The drainage of foamy granular suspensions, *Journal of Colloid and Interface Science*. 458 (2015) 200–208. doi:10.1016/j.jcis.2015.07.051.
- [32] Y. Khidas, B. Haffner, O. Pitois, Capture-induced transition in foamy suspensions., *Soft Matter*. 10 (2014) 4137–4141. doi:10.1039/c4sm00246f.
- [33] B. Haffner, Y. Khidas, O. Pitois, Flow and jamming of granular suspensions in foams., *Soft Matter*. 10 (2014) 3277–3283. doi:10.1039/c4sm00049h.
- [34] N. Louvet, R. Höhler, O. Pitois, Capture of particles in soft porous media, *Physical Review E*. 82 (2010) 041405.
- [35] F. Rouyer, O. Pitois, E. Lorenceau, N. Louvet, Permeability of a bubble assembly: From the very dry to the wet limit, *Physics of Fluids*. 22 (2010) 043302. doi:10.1063/1.3364038.
- [36] I.M. Krieger, T.J. Dougherty, A Mechanism for Non-Newtonian Flow in Suspensions of Rigid Spheres, *Journal of Rheology*. 3 (1959) 137–154. doi:10.1122/1.548848.
- [37] S. Mueller, E.W. Llewellyn, H.M. Mader, The rheology of suspensions of solid particles, *Proc. R. Soc. A*. 466 (2010) 291–300. doi:10.1098/rspa.2009.0445.